ISSN 0915-633X

NATIONAL INSTITUTE FOR FUSION SCIENCE

Computer Simulation of a Magnetohydrodynamic Dynamo II

A. Kageyama, T. Sato and The Complexity Simulation Group

(Received - Oct. 18, 1994)

NIFS-320 Nov. 1994

RESEARCH REPORT
NIFS Series

NAGOYA, JAPAN

Computer Simulation of a Magnetohydrodynamic Dynamo II

Akira Kageyama, Tetsuya Sato
and
The Complexity Simulation Group[†]

Theory and Computer Simulation Center,
National Institute for Fusion Science, Nagoya 464-01, Japan

Abstract

We performed a computer simulation of a magnetohydrodynamic dynamo in a rapidly rotating spherical shell. Extensive parameter runs are carried out changing the electrical resistivity. It is found that the total magnetic energy can grow more than ten times larger than the total kinetic energy of the convection motion when the resistivity is sufficiently small. When the resistivity is relatively large and the magnetic energy is comparable or smaller than the kinetic energy, the convection motion maintains its well-organized structure. However, when the resistivity is small and the magnetic energy becomes larger than the kinetic energy, the well-organized convection motion is highly disturbed. The generated magnetic field is organized as a set of flux tubes which can be divided into two categories. The magnetic field component parallel to the rotation axis tends to be confined inside the anticyclonic columnar convection cells. On the other hand, the component perpendicular to the rotation axis is confined outside the convection cells.

keywords: MHD dynamo, geomagnetic field, solar magnetic field

---

[†]K. Watanabe, R. Horiuchi, T. Hayashi, Y. Todo, T. H. Watanabe, and H. Takamaru

1 Introduction

In the previous paper we investigated the thermal convection in a rapidly rotating spherical shell without the magnetic field. The velocity field of the convection motion under a strong constraint of the Coriolis force was studied in detail through a computer simulation. In this paper, we proceed to the next stage of our magnetohydrodynamic (MHD) dynamo research where the behavior of the magnetic field is included. The numerical code is improved so as to solve the MHD equations in the geometry of the spherical shell. Using this code, we study the coupling between the thermal convection of an electrically conducting fluid in a rapidly rotating spherical shell and the magnetic field. Time development of the magnetic field as well as the fluid motion is self-consistently followed including all nonlinear couplings. In this paper we report our first results obtained by a full nonlinear MHD simulation.

The MHD dynamo is an energy transformation process from the kinetic energy of an electrically conducting fluid into the magnetic energy. The earth's magnetic field (geomagnetic field) and the solar magnetic field are the well-known and fascinating examples which are thought to be caused by the MHD dynamo. There are many simple but mysterious facts of the geo- or solar-magnetic field which yet remain unresolved. For instance, why is the geomagnetic field a nearly pure dipole? (It is the very question that motivates us to this research.) And why did the dipole moment reverse many times in the earth's history? As for the sun, why does the solar magnetic

field exhibit the 22 years cycle? And why does the solar toroidal field migrate to the equator as is exhibited in the butterfly diagram?

The slowness in the development of the geo- or solar-dynamo research obviously lies in the intrinsic, strong nonlinearity of the MHD equations which makes us difficult to reveal the dynamo problem purely by an analytical method. Historically, the main stream of the dynamo study is confined in the kinematic dynamo approach where the velocity field is prescribed ignoring the feedback effect from the generated magnetic field through the $\mathbf{j} \times \mathbf{B}$ force. (The velocity field is prescribed in terms of a "proper" kinetic helicity distribution, differential rotation, and meridional circulation.) This approximation makes the electromagnetic induction equation linear. It is obvious, therefore, that the kinematic dynamo approach is not physically self-consistent. In order to reveal the real dynamo mechanism, obviously we have to solve the full set of the MHD equations including all nonlinear terms. The numerical simulation using a current supercomputer enables us to deal with the full nonlinear MHD dynamo.

The numerical simulation of the full nonlinear MHD dynamo was pioneered by Gilman and Miller [1] in 1981. Their purpose was to reproduce the characteristic features of the observed solar magnetic field, especially the 22-years cycle and the equatorial migration of the toroidal field. They showed for the first time that the magnetic field could certainly be generated by the MHD dynamo in a self-consistently solved velocity field. Adopting the Boussinesq approximation, they solved the equations in the spherical

coordinate system (15 (radial) $\times$ 50 (latitudinal)) with the Fourier mode expansion in the azimuthal direction (15 modes). They, however, did not solve high latitude regions ($> 75°$ N and S) because the concentrated grid points near the north and south poles make the Courant-Friedrich-Levy (CFL) condition quite severe to fulfill. They determined the physical parameters (the Rayleigh number, Taylor number, Prandtl number, shell depth) so as to reproduce the characteristic features of the observed solar convection, especially the differential rotation profile on the surface. They carried out three parameter runs with different electrical resistivities (the magnetic Prandtl number $q = 0.1$, 0.2 and 0.4). They showed that when the resistivity was sufficiently small ($q = 0.1$ or 0.2), the seed magnetic field grew by the dynamo process. The maximum value of the magnetic energy was about 20% for $q = 0.1$ and three orders of magnitude smaller than the total kinetic energy of the convection motion for $q = 0.2$. The spatial resolution of their numerical code was not sufficiently high to simulate the dynamo with smaller resistivity or with stronger magnetic field. In both cases of $q = 0.1$ and 0.2, the spectrum of the magnetic field in their simulation was broad. In other words, the magnetic field had no particular structure.

Glatzmaier [2, 3, 4] improved the simulation model of the solar dynamo by Gilman and Miller. He developed a new code [2] in which variables are expanded by the spherical harmonics. The spherical harmonic expansion excludes the numerical difficulty arising from the CFL condition near the poles. Therefore he could solve equations in the full spherical shell. And he

used an anelastic approximation instead of the Boussinesq approximation. The anelastic approximation makes it possible to include the effects of the density stratification. He made an extensive analysis of the generated field and obtained a lot of fruitful results. However, the generated magnetic fields in his simulation were also very weak: The magnetic energy is about three orders of magnitude smaller than the kinetic energy of the convection motion.

It should be stressed that the purpose of Gilman & Miller and Glatzmaier was to reproduce the basic characteristics of the observed solar magnetic field. Therefore they chose the physical parameters as close as the values of the sun. We believe that this choice made their simulation results not so conclusive.

We performed a simulation of the MHD dynamo with rather different purpose. Our purpose is to get essential and basic ideas of fundamental MHD dynamo physics. In other words, we do not intend to compare directly our simulation results with the actual geo- or solar-magnetic field. We believe that this is the necessary first step of the dynamo research. Therefore we exclude all ad hoc assumptions. For example, we solve the full compressibility of the fluid. (We adopt neither the Boussinesq nor the anelastic approximation.)

We developed a new code in which the finite difference method is used in all directions in the spherical coordinate system. Using this code, we can solve equations in the high latitude region including the pole as well as the low latitude region. The model and numerical techniques to overcome the CFL condition problem near the pole will be described in section 2. We will

show in section 3 that the magnetic energy can reach more than ten times larger than the total kinetic energy of the convection motion. As far as we know, this kind of strong field generation has not been reported so far. New findings obtained by the analysis of the strong magnetic field will be reported and summarized in section 3 and section 4.

2 Model

2.1 Physical system and equations

The physical system, which is basically the same as that in the previous paper except for the inclusion of the magnetic field, is briefly reproduced here. We consider a spherical shell vessel bounded by two concentric spheres. An electrically conducting fluid is confined in this shell. Both the inner and outer spherical boundaries rotate with a constant angular velocity Ω. We use a rotating flame of reference with the same angular velocity. There is a central gravity force in the direction of the center of the spheres. The temperatures of both the inner and outer spheres are fixed; hot (inner) and cold (outer). Since the temperature difference between them is sufficiently large, a convection motion starts to be driven when a random temperature perturbation is imposed at the beginning of the calculation. At the same time an infinitesimally small "seed" magnetic field is given in the form of a superposition of random perturbations of a vector potential.

The system is described by the following MHD equations:

$$\frac{\partial \rho}{\partial t} = -\nabla \cdot (\rho \mathbf{v}), \tag{1}$$

$$\rho \frac{d\mathbf{v}}{dt} = -\nabla p + \mathbf{j} \times \mathbf{B} + \rho \mathbf{g} + 2\rho \mathbf{v} \times \mathbf{\Omega} + \mu(\nabla^2 \mathbf{v} + \frac{1}{3}\nabla(\nabla \cdot \mathbf{v})), \tag{2}$$

$$\frac{1}{(\gamma - 1)}\frac{dp}{dt} = -\frac{\gamma}{\gamma - 1} p \nabla \cdot \mathbf{v} + K\nabla^2 T + \eta \mathbf{j}^2 + \Phi, \tag{3}$$

$$\frac{\partial \mathbf{A}}{\partial t} = -\mathbf{E}, \tag{4}$$

with

$$p = \rho T, \tag{5}$$

$$\mathbf{B} = \nabla \times \mathbf{A}, \tag{6}$$

$$\mathbf{j} = \nabla \times \mathbf{B}, \tag{7}$$

$$\mathbf{E} = -\mathbf{v} \times \mathbf{B} + \eta \mathbf{j}, \tag{8}$$

$$\mathbf{g} = -\frac{g_0}{r^2}\hat{\mathbf{r}}, \tag{9}$$

$$\Phi = 2\mu \left(e_{ij} e_{ij} - \frac{1}{3}(\nabla \cdot \mathbf{v})^2 \right), \tag{10}$$

$$e_{ij} = \frac{1}{2}\left(\frac{\partial v_i}{\partial x_j} + \frac{\partial v_j}{\partial x_i} \right). \tag{11}$$

Here the density ρ, pressure p, velocity $\mathbf{v}$, magnetic field $\mathbf{B}$ are independent variables. $\mathbf{A}$, $\mathbf{j}$ and $\mathbf{E}$ are the vector potential, the current density and the electric field, respectively. The ratio of the specific heats $\gamma(= 5/3)$, the viscosity μ, the thermal conductivity K and the electrical resistivity η are assumed to be constant. g is the gravity acceleration and $\hat{\mathbf{r}}$ is the radial unit vector. g_0 is a constant.

We normalize the quantities as follows: The radius of the outer sphere $r_o = 1$; the temperature of the outer sphere $T(r_o) = 1$; and the mass density at the outer sphere $\rho(r_o) = 1$. The normalization units of other variables are given by combinations of these variables [5]. The gravity is inversely proportional to the square force since we ignore the self gravity of the fluid. We also ignore the centrifugal force in the equation of motion (2) by assuming that it is absorbed into the gravity field.

2.2 Coordinate system and numerical method

The above equations are numerically solved in a spherical coordinate system (r, ϑ, φ), where r is the radius, ϑ is the colatitude and φ is the longitude. The polar axis $\vartheta = 0$ is taken to be the direction of the angular velocity vector $\mathbf{\Omega}$. We call the plane $\vartheta = \pi/2$ the equatorial plane.

It is well known that the velocity field of the convection motion without any magnetic field is symmetric about the equatorial plane when the rotation rate of the spherical shell is sufficiently high. This symmetrical motion is confirmed in our previous paper. We have made several preliminary MHD simulations in which the equations are solved in the full spherical shell region $(0 \leq \vartheta \leq \pi)$. We have found that the generated magnetic field is always nearly anti-mirror symmetric about the equator [3]. Accordingly, we solve in this paper only a half hemisphere by assuming the anti-mirror symmetry for the magnetic field and the mirror symmetry for other variables ($\mathbf{v}$, p, ρ). Hence, the magnetic field on the equatorial plane has only the normal

(latitudinal) component ($B_r = B_\varphi = 0$).

As we did in the previous paper we use the second-order finite difference in all directions (r, ϑ and φ) and the fourth-order Runge-Kutta-Gill (RKG) method for the time integration. The grid numbers are 30 (radial), 32 (latitude; $0 \leq \vartheta \leq \pi/2$) and 128 (longitude; $0 \leq \varphi < 2\pi$), respectively.

2.3 Initial and boundary conditions

The initial condition is given by a hydrostatic and thermal equilibrium state:

$$T(r) = 1 - \beta + \frac{\beta}{r}, \tag{12}$$

$$\rho(r) = T(r)^m, \tag{13}$$

with

$$\mathbf{v} = 0, \tag{14}$$

and

$$\mathbf{B} = 0, \tag{15}$$

where $\beta > 0$ is a constant and

$$m = \frac{g_0}{\beta} - 1 \tag{16}$$

is the polytropic index.

The temperatures at both the inner ($r = r_i$) and outer ($r = r_o = 1$) boundaries are fixed. A rigid boundary condition is given for the velocity:

$$\mathbf{v} = 0 \qquad \text{at } r = r_i, 1. \tag{17}$$

For the magnetic field, we adopt the following boundary conditions which are exactly the same as those of Gilman and Miller [1]:

$$E_\vartheta = E_\varphi = 0 \qquad \text{at } r = r_i, \tag{18}$$

and

$$E_r = \frac{\partial}{\partial r}(rE_\vartheta) = \frac{\partial}{\partial r}(rE_\varphi) = 0 \qquad \text{at } r = 1. \tag{19}$$

The condition (18) means that the inner spherical boundary is a perfect conductor. And the condition (19) means that the radial component of the magnetic field can diffuse out through the outer spherical boundary. ($B_\vartheta = B_\varphi = 0$ but $B_r \neq 0$ at $r = 1$). This implies that there is no Poynting flux ($\mathbf{E} \times \mathbf{B}$) through the outer boundary as is the case for the inner perfect conductor boundary. By imposing this no Poynting flux entry condition through the boundaries, we can definitely conclude that any magnetic field, if generated, must be a consequence of the dynamo action in the bulk of the spherical shell.

2.4 Physical parameters

The system has seven free parameters: r_i (radius of the inner sphere), μ, K, η, g_0, Ω and m. It is practically impossible to perform a comprehensive parameter study to cover the whole seven dimensional parameter space. Therefore we confine ourselves to an extensive parameter run in one dimensional subspace of the resistivity η. This is because the resistivity is supposed to be the most interesting and important parameter in the generation process

of the magnetic field.

The other parameters are chosen so that they can be representative of the following two principles for the convection motion with no magnetic field: (i) The convection motion keeps a well-organized (non-turbulent) global structure and (ii) the convection motion is strongly constrained by the Coriolis force. The latter condition (ii) can be visually confirmed when the columnar convection cells, which we call in this paper "convection columns [5]", are regularly formed in the longitudinal direction and stand straight along the rotation axis. The above two conditions can be rephrased as: (i') The Rayleigh number R should not be so large compared with the critical value R_c. (ii') The Taylor number T should be taken as large as possible.

The actual procedure to find a proper set of parameters is quite complicated because the critical Rayleigh number R_c depends on the Taylor number T. And both R and T are not independent parameters in the present compressible convection system. Moreover, there remains a large freedom in the choice of the parameters which satisfy the above conditions. Hence, we impose one more condition which comes from a rather computational reason. Evidently, the dynamo efficiency strongly depends on the convection velocity (see equations (4) and (8)). If the convection velocity is too slow, it will take a lot of calculation time to follow the time development of the system. If the convection velocity is too fast (e.g., supersonic), on the other hand, the role of the compressibility of the fluid would become sizable. The influence of the compressibility on the dynamo action is another (and probably more

difficult) subject of the MHD dynamo. This is beyond the scope of this paper. At our own choice, therefore, we set the convection velocity to be about 10% of the sound velocity.

We have made a lot of parameter runs in order to find a proper set of parameters that satisfy the above conditions. The chosen parameters are as follows: $r_i = 0.3$, $\mu = 2.829 \times 10^{-3}$, $K = 2.423 \times 10^{-3}$, $g_0 = 1.0$, $\Omega = 7$ and $m = 0.25$. In this case, the Taylor number and the Rayleigh number are $T = 5.88 \times 10^6$ and $R = 2.00 \times 10^4$, respectively. Under these fixed parameters, we carry out eight simulations with different resistivity η: $\eta = 1 \times 10^{-5}$, 6×10^{-5}, 8×10^{-5}, 1×10^{-4}, 1.2×10^{-4}, 1.4×10^{-4}, 2×10^{-4} and 4×10^{-4}.

2.5 Numerical techniques

There are two numerical difficulties in solving the finite difference equations on the spherical coordinate system. One is the severe CFL condition on the time step due to the concentrated grid points near the pole and the other is the "singularity" on the pole. The first difficulty is successfully overcome by a devised smoothing procedure near the pole. This smoothing procedure is described in the previous paper [5]. In this respect, it will be a good place to explain the reason that we have used the vector potential $\mathbf{A}$ in the electromagnetic induction equation (4). When we use the magnetic field $\mathbf{B}$ in the induction equation as usual, the smoothing procedure has to be applied to $\mathbf{B}$. Then, the smoothing procedure produces an artificial

magnetic monopole component ($\nabla \cdot \mathbf{B} \neq 0$), although its magnitude is very small. The numerical production of the monopole component should be taken as a serious problem especially in the MHD dynamo study. When we use the vector potential $\mathbf{A}$ in the induction equation, the smoothing procedure does work quite satisfactorily. The magnetic field is then calculated by the equation (6). This magnetic field exactly satisfies the equation $\nabla \cdot \mathbf{B} = 0$ because the equation $\nabla \cdot \nabla \times \mathbf{A} = 0$ is rigidly satisfied in the finite difference equation in the spherical coordinate system.

As for the pole singularity problem, we have adopted a more sophisticated method than the previous one. The "singularity" of the MHD equations on the pole in the spherical coordinate system is removed by the use of the following theorem [6]:

$$\text{if} \quad \lim_{\vartheta \to 0} f(\vartheta) = \lim_{\vartheta \to 0} g(\vartheta) = 0 \quad \text{then} \quad \lim_{\vartheta \to 0} \frac{f(\vartheta)}{g(\vartheta)} = \lim_{\vartheta \to 0} \frac{f'(\vartheta)}{g'(\vartheta)}, \tag{20}$$

where the prime denotes the derivative. The MHD equations on the pole ($\vartheta = 0$) can be transformed into a non-singular form by this theorem. We place grid points on the pole ($\vartheta = 0$) and solve the transformed MHD equations on these grids by the finite difference method.

3 Results

3.1 Magnetic field generation

We first make the "basis simulation" in which the convection motion is fully calculated with no effect of the magnetic field included ($\mathbf{B} = 0$). Then we perform eight simulations with different resistivities.

Fig. 1 shows the time development of the magnetic energy (ME) with different resistivities η. The time development of the total kinetic energy (KE) of the basis case is also shown (the solid line in Fig. 1). The magnetic field is amplified in all the cases except for the largest η ($= 4 \times 10^{-4}$). The curve for $\eta = 2 \times 10^{-4}$, which is nearly horizontal, indicates that the threshold of the resistivity for the field amplification is a little larger than this value in the present parameter range.

It is evident that the smaller the resistivity, the larger the saturated magnetic energy. This is of course due to the small resistive dissipation. The most striking point discovered in our simulation is that the magnetic energy for the smallest resistivity ($\eta = 1 \times 10^{-5}$) reaches more than ten times larger than the total kinetic energy (see the upper most curve in Fig. 1). To our knowledge, this is the first MHD dynamo simulation that has demonstrated the generation of such a strong magnetic field.

It is also shown in Fig. 1 that the smaller the resistivity, the smaller the time for getting a saturation level. There is an exponential growth phase of the ME for each resistivity case. The relation between the growth rate γ and

the resistivity is given in Fig. 2. This graph shows that the positive growth rate, which means the field amplification rate, lies on a linear function of the logarithm of the resistivity: $\gamma = -c_1 \log \eta + c_2$, where c_1 and c_2 are constants.

For $\eta < 1 \times 10^{-4}$, ME is larger than KE, while for $\eta > 1 \times 10^{-4}$, ME is smaller than KE. The curve for $\eta = 1 \times 10^{-4}$ in Fig. 1 suggests that this value is just "critical". We will show later that the convection motion exhibits a qualitatively different behavior depending on whether ME > KE or ME < KE. It will also be shown that the convection motion with the critical $\eta = 1 \times 10^{-4}$ shows an interesting behavior.

3.2 Convection motion with the magnetic field

The circles in Fig. 3 show the KE at the end of run for different resistivities. For comparison, the KE of the basis case is indicated by the dashed horizontal line. The asterisk mark in Fig. 3 denotes the ME. It is seen that the KE stays the same level as the basis run even if the ME is larger than the KE. It is to be noted here that we may be able to get a larger magnetic field for a smaller resistivity than $\eta = 10^{-5}$, but that such a strong magnetic field is practically difficult to get by the present simulation because the numerical time step Δt which is restricted by the magnetosonic velocity becomes impracticably small.

Although the KE remains almost the same level for all the resistivity cases, the qualitative character of the velocity field illustrates a remarkable difference. When ME > KE (i.e., $\eta < 1 \times 10^{-4}$), the convection motion

becomes turbulent, while when ME < KE, the convection motion keeps its original laminar pattern. This is a kind of transition of the convection motion induced by the magnetic field. This transition is very sensitive to the condition of whether ME > KE or not. One of the features of the transition appears in the temporal fluctuation of the level of the KE. Note that there appears no fluctuation for the level of the KE in the basis case (see the rigid line in Fig. 1). We plot the kinetic energies at ten arbitrary times after the saturation of the ME in Fig. 4. The dashed line denotes the KE of the basis case. One can clearly see that when $\eta \leq 1 \times 10^{-4}$ (ME $\geq$ KE), the temporal fluctuation of the KE is quite large. On the other hand, the fluctuation is very small for $\eta > 1 \times 10^{-4}$ (ME < KE).

The transition of the convection motion is more clearly visualized in Fig. 5(a) to (f) where (a) basis case, (b) $\eta = 1 \times 10^{-5}$, (c) $\eta = 8 \times 10^{-5}$, (d) $\eta = 1 \times 10^{-4}$, (e) $\eta = 1.2 \times 10^{-4}$ and (f) $\eta = 1.4 \times 10^{-4}$. In these figures, the temporal development of the convection columns are presented. The horizontal axis of Fig. 5 is the longitude ($0° \leq \varphi < 360°$) and the vertical axis is the time. The black region denotes the rising fluid ($v_r > 0$) in the equatorial plane at $r = 0.65$ and the white region denotes the sinking fluid ($v_r < 0$). The pairs of the black and the white regions at each time correspond to the pairs of convection columns.

We first examine the basis case. After a short initial growing phase ($t <$ 50) the convection motion reaches a stationary state and keeps its regular motion thereafter. There are six pairs of convection columns which drift

"westward", i.e., the opposite direction of the spherical rotation.

In Fig. 5(b), the convection columns drift westward until $t \simeq 3 \times 10^2$ at which time the ME exceeds the level of the KE (see Fig. 1). Up to this time, the behavior of the convection columns (the uniform westward drift) keeps almost the same behavior as that of the basis case, since the $\mathbf{j} \times \mathbf{B}$ force is too weak to affect the convection motion. However, at about $t = 3 \times 10^2$, the magnetic field begins to change the drift velocity of the columns. The direction of the longitudinal drift motion of the columns is reversed (eastward drift) at about $t = 3.9 \times 10^2$. The regular stripe pattern disappears after $t \simeq 6 \times 10^2$ at which time the ME almost saturates (see Fig. 1). The pattern after $t \simeq 6 \times 10^2$ suggests that the convection motion becomes turbulent.

Fig. 5(c) shows the case for $\eta = 8 \times 10^{-5}$. The initial temporal evolution of the six pairs of columns remains the same as that of the basis case (Fig. 5(a)) until $t \simeq 7 \times 10^2$ at which time the ME reaches to the same level of the KE (see Fig. 1). As is observed in the case of Fig. 5(b), the drift motion of the columns becomes eastward after the ME exceeds the KE. The stripe pattern in Fig. 5(c) indicates that the number of convection columns decreases from six to five at $t \simeq 1.1 \times 10^3$. It is also seen that the column number changes several times, though the drift direction keeps eastward. The convection motion also becomes turbulent, although the fluctuation is not so large as is seen in Fig. 5(b). A similar behavior is observed for the case of $\eta = 6 \times 10^{-5}$, which is not presented here, though. The major difference is that the drift direction is reversed at $t = 6 \times 10^2$ when the ME reaches the KE (see Fig. 1).

It is interesting to examine the case of the "critical resistivity" ($\eta = 1 \times 10^{-4}$; Fig. 5(d)). The effect of the magnetic field appears at $t \simeq 1 \times 10^3$ when the ME reaches the KE. The "column number transition" is recognized at $t \simeq 1.1 \times 10^3$ in Fig. 5(d). At this time the convection columns, which initially consists of six pairs, are divided into eight pairs. The eight pairs of columns are almost the same in size and they drift westward with the same phase velocity as that when they used to be six (compare the angles of the stripe patterns). It should be noted that the ME rapidly drops at $t \simeq 1.1 \times 10^3$ (see the graph of $\eta = 1 \times 10^{-4}$ in Fig. 1). This seems to suggest that the reconstruction of the convection columns consumes the ME. Fig. 1 indicates that the ME reaches again the same level of the KE at $t \simeq 1.6 \times 10^3$. The second column number transition takes place at this time (see Fig. 5(d)). The number of the column pairs becomes seven after this transition.

Fig. 5(e) shows the behavior for $\eta = 1.2 \times 10^{-4}$ in which case the ME is always less than the KE (see Fig. 1). The stripe pattern in Fig. 5(e) is almost identical to that of Fig. 5(a), i.e., for the convection motion without the magnetic field. The time development of the ME for $\eta = 1.2 \times 10^{-4}$ in Fig. 1 indicates that the ME reaches about 10% of the KE after $t \simeq 1.4 \times 10^3$. Although the ME is certainly less than the KE, such a magnetic field may have some effect on the convection motion. However, any distinct indication of the effect of the magnetic field is recognized after $t \simeq 1.4 \times 10^3$. (One can find, however, from a detailed comparison between Fig. 5(a) and Fig. 5(d) that the column drift velocity is a little slowed down by the magnetic field.)

It will be confirmed later that the convection motion for $\eta = 1.2 \times 10^{-4}$ is almost identical to that of the basis case.

The observed robustness of the convection motion against the presence of the magnetic field in our study makes a contrast with the results of Gilman and Miller [1]. They found that the convection motion was very sensitive to the presence of the magnetic field. Even a very weak magnetic field (by three orders of magnitude smaller than the kinetic energy) does significantly affect the convection motion in their simulation. The robustness in our simulation apparently comes from the choice of the high Taylor number. The rapid rotation makes the Coriolis constraint on the fluid flow quite strong. Therefore the convection motion is quite stable in our case. On the other hand, Gilman and Miller chose a relatively low Taylor number comparered with their high Rayleigh number. This must make the fluid motion sensitive to the existence of the magnetic field, whatever small it is.

In order to visualize the three dimensional structure of the velocity field, the isosurfaces of the axial component of vorticity $\omega_Z = \omega \cdot \mathbf{\Omega}/\Omega$ are illustrated in Fig. 6. The panels (a), (a') and (a") show the isosurfaces for $\eta = 1.2 \times 10^{-4}$. The three panels show the same object but viewed from different directions; (a) from the north pole $\vartheta = 0$, (a') from $\vartheta = 45°$ and (a") from $\vartheta = \pi/2$, i.e., the equator. The panels (b) to (b") and (c) to (c") show the isosurfaces for $\eta = 1 \times 10^{-4}$ and $\eta = 1 \times 10^{-5}$. The viewing angles are the same as those of (a) to (a"). The six pairs of convection columns are clearly seen in Fig. 6(a) to (a"). We have plotted the isosurface for the basis case to find that it is

identical to those of Fig. 6(a) to (a"). This provides another evidence that the velocity field of the convection motion for $\eta = 1.2 \times 10^{-4}$ is almost the same as that of the basis case.

We saw previously in Fig. 5(c) that the number of the convection column pairs became seven when $\eta = 1 \times 10^{-4}$ after the second transition. The seven pairs of the convection columns are visualized in Fig. 6(b) to (b"). The profile of the convection columns in Fig. 6(b) to (b") are quite similar to that in Fig. 6(a) to (a"). The velocity structure is essentially the same as that of the basis case. The only difference is the longitudinal mode number. A remarkable point to be noted in Fig. 6(b) to (b") is that the convection motion is still laminar in spite of the presence of the strong magnetic field (ME $\sim$ KE). The temporal fluctuation of the KE for $\eta = 1 \times 10^{-4}$ shown in Fig. 4 comes from the rapid energy rise and fall phenomena which appear only when the "column number transition" takes place. The same behavior is also seen in Fig. 5(d). On the other hand, the KE of the cases for $\eta < 1 \times 10^{-4}$ fluctuates rather randomly after the ME becomes larger than the KE.

In Fig. 6(c) to (c"), it is observed that the regular structure of the convection columns is destroyed. This figure indicates that the convection motion becomes more or less turbulent, although there still remain some residuals of the columnar structure of the convection motion.

From the above results we can conclude that the convection motion is largely dependent on the condition of whether the ME > KE or not. As far as the ME stays less than the KE, the convection motion remains almost

the same as that for no magnetic field. When the ME grows larger than the KE, however, the convection motion is greatly disturbed and becomes more turbulent.

3.3 Structure of the magnetic field

We are now at the position of examining the structure of the generated magnetic field. By having examined the structures for all cases, we have found that the basic characteristics of the magnetic field structures are almost the same except for the magnitudes of the generated fields. In what follows, therefore, we concentrate our attention to the results for $\eta = 1 \times 10^{-5}$, since the generated magnetic field is the strongest. The results for $\eta = 1.4 \times 10^{-4}$, in which the magnetic energy is less than the kinetic energy, are also presented for comparison.

The latitudinal component of the magnetic field B_ϑ in the equator at the end of the run for $\eta = 1 \times 10^{-5}$ ($t = 1.76 \times 10^3$) is shown in Fig. 7(a). Note that other components of the magnetic field are absent owing to the boundary condition. For comparison, the velocity field is shown in Fig. 7(b) where for brevity the velocity arrows are plotted only on every four grid points. Examination of the radial distribution of the magnetic energy density indicates that there is a thin layer of the concentrated magnetic field between $r = 0.3$ (inner boundary) and $r \simeq 0.33$ which is sandwiched between the inner envelope of the convection columns and the perfectly conducting inner spherical boundary. However, the contribution of the magnetic energy in

the boundary layer to the total magnetic energy is only 5.5% of the total magnetic energy in the system. For clarity, therefore, the magnetic field in the boundary layer is not shown in Fig. 7(a).

By comparison between Fig. 7(a) and (b) one notices that there are three magnetic fluxes which are confined in the centers of the anticyclonic convection columns. (Fluids in an anticyclonic column rotate in the opposite direction of the spherical shell; clockwise in Fig. 7.) Let us then investigate the three dimensional structure of the magnetic field. For convenience, we divide the total volume of the spherical shell V into two regions V_1 and V_2. Here V_1 is defined as the region $R \leq 0.3$ where R is the distance from the rotation axis. (In what follows, the cylindrical coordinate system (R, φ, z) is used, where the z-axis coincides with the $\vartheta = 0$ direction in the spherical coordinate system.) Thus, the region V_1 is the "polar region". The magnetic field in V_1 is relatively weak and complicated. Thus, we are not interested in it. On the other hand, the magnetic field in V_2 has a distinct structure. It is organized as discrete flux tubes. A careful examination of the simulation data tells us that there are two kinds of the flux tubes, which can be distinguished by the z-component of the magnetic field. Accordingly, we divide the magnetic energy W into two parts: $W \equiv \mathbf{B}^2/2 = W_Z + W_\perp$, where $W_Z \equiv {B_Z}^2/2$ and $W_\perp \equiv {B_\perp}^2/2 \equiv {B_R}^2/2 + {B_\varphi}^2/2$. Then, the two kinds of flux tubes can be visualized by the isosurfaces of W_Z and $W_\perp$.

We first show the flux tubes of the magnetic field parallel to the z-axis. Fig. 8(a) and (b) illustrate the isosurfaces of $W_Z = 0.03$ at $t = 1.76 \times 10^3$

($\eta = 1 \times 10^{-5}$), which are viewed from two different angles; (a) from $\vartheta = 45°$ and (b) 90° (equator). The gray disk in Fig. 8 denotes the equatorial plane. The maximum value of W_Z is 0.989 and the region in which $W_Z \geq 0.03$ is 1.13% of the total volume of V_2. In order to elucidate the relative position of the isosurfaces to the convection columns, they are colored with yellow or blue depending on the value of the z-component of the vorticity ω_Z. It should be noted that the amplitude of ω_Z is large in convection columns, particularly, a strong positive (negative) ω_Z corresponds to a cyclonic (anticyclonic) convection column. The isosurface with $\omega_Z \geq 0.4$ ($\omega \leq -0.4$) is colored with blue (yellow) and others are white. One can recognize from Fig. 8 that the blue region is almost null but that the most part of the isosurfaces are yellow and are nearly parallel to the z-axis. There are three yellow columnar magnetic flux tubes. The "yellow" color means that they are confined in the anticyclonic columns. The magnetic fluxes shown in Fig. 7(a) correspond to these three flux tubes. The phenomenon of the B_z flux confinement in the anticyclonic columns is also seen in other resistivity cases. For example, there are four confined flux tubes for $\eta = 1.4 \times 10^{-4}$.

We shall move onto the other kind of the flux tube. Fig. 9(a) to (d) show the isosurfaces of $W_\perp = 0.03$ for the case of $\eta = 1 \times 10^{-5}$, i.e., the flux tubes of the magnetic field perpendicular to the z-axis. The viewing angles of Fig. 9(a) to (d) are as follows: (a) from $\vartheta = 0$ (north pole), (b) 30°, (c) 60° and (d) 90° (equator). The isosurfaces in Fig. 9 are also colored with blue or yellow depending on the vorticity ω_Z at each point. The threshold value and

the meaning of the colors are also the same as those in Fig. 8. Fig. 9 shows that the most part of the isosurfaces are white. This means that these flux tubes are located outside the convection columns.

The radial profile of the magnetic energy density in a stationary state for $\eta = 1.4 \times 10^{-4}$ is given in Fig. 10 (dashed line) which indicates that a rather strong magnetic field exists near the outer spherical boundary ($r > 0.7$). From equations (4), (6) and (8), the time development of the magnetic energy density can be written as follows;

$$\frac{\partial}{\partial t}(\mathbf{B}^2/2) = -\mathbf{v} \cdot (\mathbf{j} \times \mathbf{B}) - \nabla \cdot (\mathbf{E} \times \mathbf{B}) - \eta \mathbf{j}^2. \tag{21}$$

The solid curve in Fig. 10 denotes the profile of the energy transport due to the Poynting flux in the radial direction, which is given by integrating the second term in the right hand side of the equation (21) over ϑ and φ. The solid curve is negative in $r < 0.7$ where the dynamo term $-\mathbf{v}\cdot(\mathbf{j}\times\mathbf{B})$ is positive (see the dotted line in Fig. 10). This indicates a tendency that the generated energy is transferred from this region to outside by the Poynting flux. On the other hand, the solid curve becomes positive in $r > 0.7$, where the dynamo term rapidly decreases. This implies that the transferred magnetic energy is accumulated in $r > 0.7$. Consequently, one can conclude that the strong magnetic field near the outer spherical boundary is maintained by the energy transport from the inner region $r < 0.7$.

Let us briefly summarize the above results. The strong magnetic field generated by the MHD dynamo is organized as discrete flux tubes. The

magnetic fields parallel to the z-axis are confined mainly in the anticyclonic columns, while the magnetic fields perpendicular to the z-axis are confined outside the convection columns. We shall discuss in section 4 the mechanism that makes such a difference in the generation of the flux tubes and attempt to find the reason that the flux tubes are confined selectively in anticyclonic columns, not in cyclonic columns.

In connection with the mean field MHD dynamo theories [7], it is interesting to examine the longitudinally averaged magnetic field $\overline{\mathbf{B}}$. Fig. 11(a) shows $\overline{B}_r$ and $\overline{B}_\vartheta$ by arrows in the meridian plane and Fig. 11(b) shows $\overline{B}_\varphi$ by contour lines. It should be remarked that no strong toroidal flux is observed in Fig. 11(b). As can be seen from Fig. 11(a), there appears a definite structure in the meridian plane for the averaged poloidal field, though the magnitude is not so strong as expected.

Here, we shall briefly comment on the dipole component emerging from the outer boundary $r = 1$ to the outside space. The magnetic field on the outer boundary is expanded into the spherical harmonics. The analysis indicates that there exists a definite amount of the dipole moment. The energy of the dipole moment is roughly 10% of the total energy for $\eta = 1.4 \times 10^{-4}$ at the end of the run.

Finally we consider the distribution of the angle ψ between the velocity $\mathbf{v}$ and the magnetic field $\mathbf{B}$ in the spherical shell (Fig. 12):

$$\psi \equiv \arccos\left(\frac{\mathbf{v}\cdot\mathbf{B}}{|\mathbf{v}||\mathbf{B}|}\right). \tag{22}$$

The rigid line denotes the distribution of the angle for $\eta = 1 \times 10^{-5}$ at the end of the run and the dotted line for the run of $\eta = 1.4 \times 10^{-4}$. If $\mathbf{v}$ and $\mathbf{B}$ distribute independently, the distribution of the angle must approach to a sin-function which is shown by the dashed line in Fig. 12. The results show that the magnetic field has a tendency to become parallel or antiparallel to the convection motion. This tendency can be understood as the magnetic field stretching effect subject to the flow of highly conducting fluids. The effect is especially strong for the case of $\eta = 1.4 \times 10^{-4}$, because the magnetic field for $\eta = 1.4 \times 10^{-4}$ is so weak and hence is strongly dependent on the fluid motion.

4 Summary and Discussion

We have performed a computer simulation of an MHD dynamo in a rapidly rotating spherical shell. Extensive parameter runs have been carried out by changing the resistivity. New results obtained by the present simulation are summarized as follows:

1. When the resistivity is sufficiently small, the magnetic energy (ME) generated by the dynamo can become larger than the kinetic energy (KE) of the convection motion. It reaches more than ten times larger than the KE.

2. The KE keeps nearly the same level irrespective of the generation of the magnetic field. This is true even for the case when the ME becomes

more than ten times larger than the KE.

3. The growth rate of the ME is well represented by a linear function of the logarithm of the resistivity. The physical process is under investigation.

4. The structure of the convection columns become quite different depending on whether the ME is larger than the KE or not.

5. When ME < KE, the convection motion keeps an almost identical motion to that of the convection motion with no magnetic field. The convection motion in this case is so robust that it is not affected by the existence of the magnetic field.

6. When ME > KE, the convection motion is strongly disturbed by the magnetic field and becomes turbulent.

7. The generated magnetic field is organized in discrete flux tubes.

8. There are two kinds of the magnetic flux tubes which can be distinguished by the contained field component. One is the B_Z–flux tube and the other is the $B_\perp$–flux tube; here z-axis is the rotation axis and the $B_\perp$ denotes the magnetic field perpendicular to the axis.

9. The B_Z flux tubes are confined in the anticyclonic columns.

10. The $B_\perp$ flux tubes are confined outside the convection columns.

The last observation can be explained by the flux expulsion effect of the MHD fluids by the convection motion parallel to the magnetic field. It is well

known from the previous two dimensional magnetoconvection studies that initially uniform magnetic field is expelled from the centers of the convection cells to the cell boundaries [8]. Magnetic field lines near the center of a convection cell are strongly wound up by the convection motion. And then the resistive disspation rate becomes quite large owing to the reduced scale lengths. Therefore the field in the center of the cells is expelled from the center of the cell. In our spherical shell convection, the fluid flow in the convection columns is almost perpendicular to the z-axis [5]. Therefore the magnetic field perpendicular to the z-axis is expelled from the convection columns.

On the other hand, the magnetic field parallel to the z-axis does not feel the flux expulsion effect by the fluid flow perpendicular to the axis in the convection columns. Then, we come to a question why the B_Z–flux is confined selectively in the anticyclonic column. In order to understand this phenomenon, we have to remember another component of the fluid flow in the convection columns, i.e., the flow parallel to the z-axis or along the column axis [5]. The flow component along the axis is always in the direction toward the equator in the cyclonic columns. On the other hand, the flow component along the axis is always in the direction away from the equator in the anticyclonic columns. Therefore there is a fluid transport near the equator *from* the cyclonic columns *to* the neighboring anticyclonic columns. The anticyclonic columns absorb fluids near the equator and convey them toward the high latitude regions by the flow along the column axis. (This

is analogous to a cyclone on the surface of the earth.) The magnetic field parallel to the z-axis is collected and confined by this absorbing flow near the equator in the anticyclonic columns. This also explains that the B_z–flux tubes are observed only near the equator (see Fig. 8).

Acknowledgements

This work is supported by the Grants-in-Aid from the Ministry of Education, Science and Culture (No. 06044238 and No. 05836038) and by the Graduate University for Advanced Study as a collaboration research. This work was performed by the Advanced Computing System for Complexity Simulation.

References

[1] P. A. Gilman and J. Miller, Astrophys. J. Suppl., **46**, 211 (1981).

[2] G. A. Glatzmaier, J. Comp. Phys., **55**, 461 (1984).

[3] G. A. Glatzmaier, Astrophys. J., **291**, 300 (1985).

[4] G. A. Glatzmaier, Geophys. Astrophys. Fluid Dynamics, **31**, 137 (1985).

[5] A. Kageyama, K. Watanabe and T. Sato, Phys. Fluids B, **8**, 2793 (1993).

[6] M. Abramowitz and I. A. Stegun ed., *Handbook of Mathematical Functions* (Dover, New York, 1964), p. 13

[7] H. K. Moffatt, *Magnetic Field Generation in Electrically Conducting Fluids*, (Cambridge Univ. Press, 1978).

[8] N.O. Weiss, Proc. Roy. Soc. London, **A 293**, 310 (1966).

Figure Captions

Fig. 1 Temporal development of the magnetic energy for eight different resistivities η. The kinetic energy (KE) of the basis case, in which the magnetic field is not included, is also shown for comparison.

Fig. 2 The circle denotes the growth rate of the magnetic energy in the initial linear growing phase for each resistivity case. The positive growth rate lies on a linear function of the logarithm of the resistivity.

Fig. 3 The kinetic energy (circle) and the magnetic energy (asterisk) at the end of each run. The dashed line denotes the kinetic energy of the basis case (without the magnetic field) in the stationary state.

Fig. 4 Fluctuations of the kinetic energy in the resistivity domain. The circles are the kinetic energies evaluated at ten different time steps after the saturation of the magnetic energy.

Fig. 5 Temporal development of a cross sectional pattern of the convection columns. The black (white) region at each time denotes the rising (sinking) fluid in the equatorial plane at $r = 0.65$. Each panel shows (a) basis case, (b) $\eta = 1 \times 10^{-5}$, (c) 8×10^{-5}, (d) 1×10^{-4}, (e) 1.2×10^{-4} and (f) 1.4×10^{-4}.

Fig. 6 Three dimensional structure of the convection columns visualized by the isosurfaces of the axial component of the vorticity ω_Z. (a), (a') and (a") show the same object viewed from different angles ($\eta = 1.2 \times 10^{-4}$); (a) from $\vartheta = 0$, i.e., the north pole, (a') from $\vartheta = \pi/4$ and (a") from $\vartheta = \pi/2$, i.e., the equator. (b) and (c) are data of $\eta = 1 \times 10^{-4}$ and $\eta = 1 \times 10^{-5}$. The panels (c) to (c") indicate that the convection motion becomes turbulent.

Fig. 7 (a) The latitudinal component of the magnetic field B_ϑ in the equatorial plane at the end of the run for $\eta = 1 \times 10^{-5}$. (b) The velocity field in the equatorial plane. Three magnetic flux tubes are confined in the anticyclonic columns.

Fig. 8 Magnetic flux tubes visualized by the isosurfaces of $W_Z = B_Z^2/2 = 0.03$ when $\eta = 1 \times 10^{-5}$. The color denotes the axial vorticity ω_Z at each point on the isosurface. The surface where $\omega_Z \geq 0.4$ ($\omega_Z \leq -0.4$) is colored with blue (yellow) and others are white. The flux tubes colored with yellow mean that these B_Z fluxes are confined in the anticyclonic columns.

Fig. 9 The flux tubes of the magnetic field perpendicular to the z-axis visualized by the isosurface of $W_\perp = 0.03$ when $\eta = 1 \times 10^{-5}$. The meaning of the colors are the same as those in Fig. 8. Major part of the isosurfaces is white. This means that these flux tubes are out of the convection columns.

Fig. 10 The radial profiles of the magnetic energy density and the energy transfer rate.

Fig. 11 Meridian cross section of the longitudinally averaged magnetic field for $\eta = 1 \times 10^{-5}$ at the end of the run.

Fig. 12 Distribution of the angle between the velocity and the magnetic field for $\eta = 1 \times 10^{-5}$ (solid line) and $\eta = 1.4 \times 10^{-4}$ (dotted line).

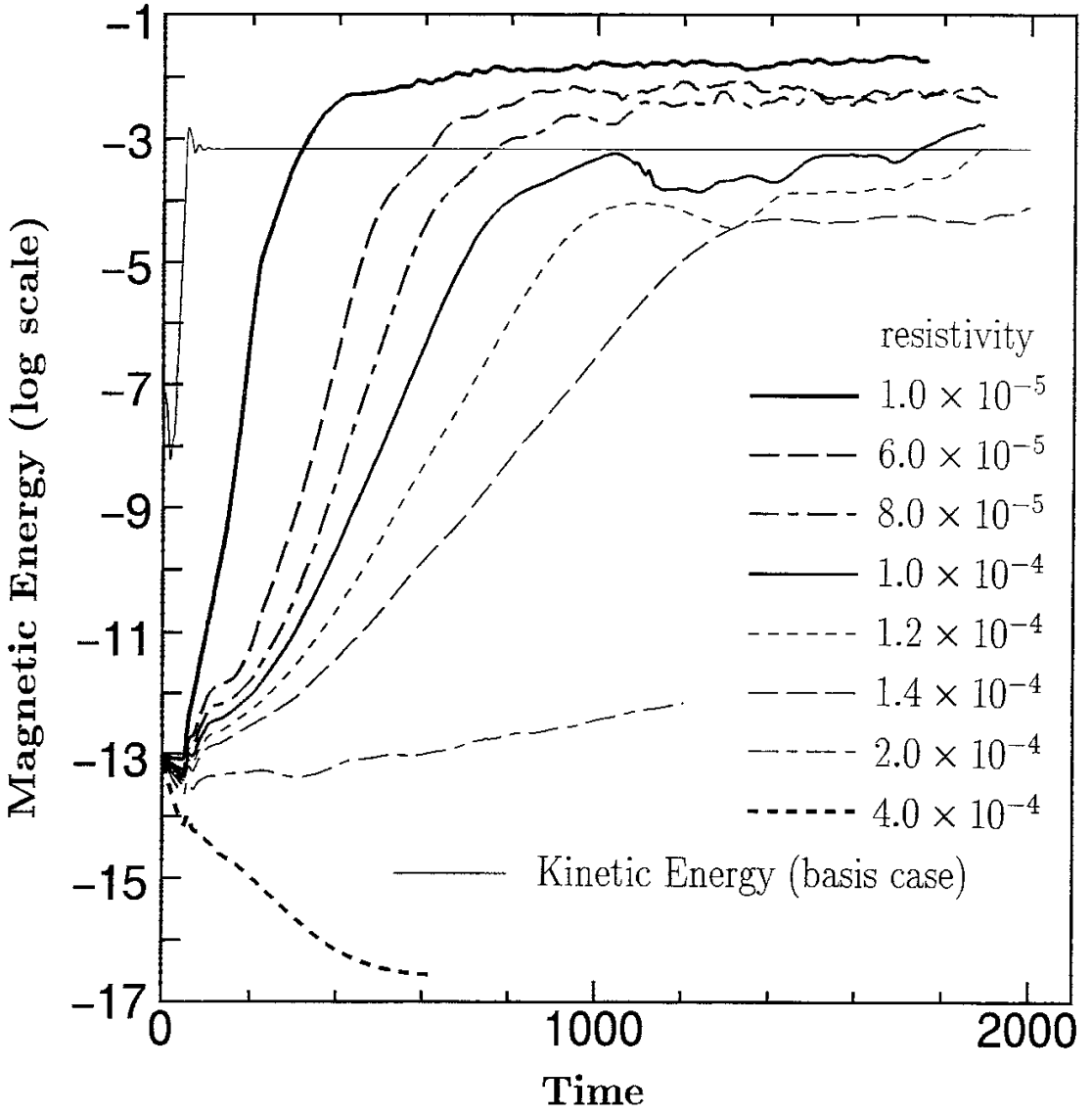
Magnetic Energy (log scale)
-1
-3
-5
-7
-9
-11
-13
-15
-17
0
1000
2000
Time
resistivity
1.0 × 10^-5
6.0 × 10^-5
8.0 × 10^-5
1.0 × 10^-4
1.2 × 10^-4
1.4 × 10^-4
2.0 × 10^-4
4.0 × 10^-4
Kinetic Energy (basis case)

Fig. 1

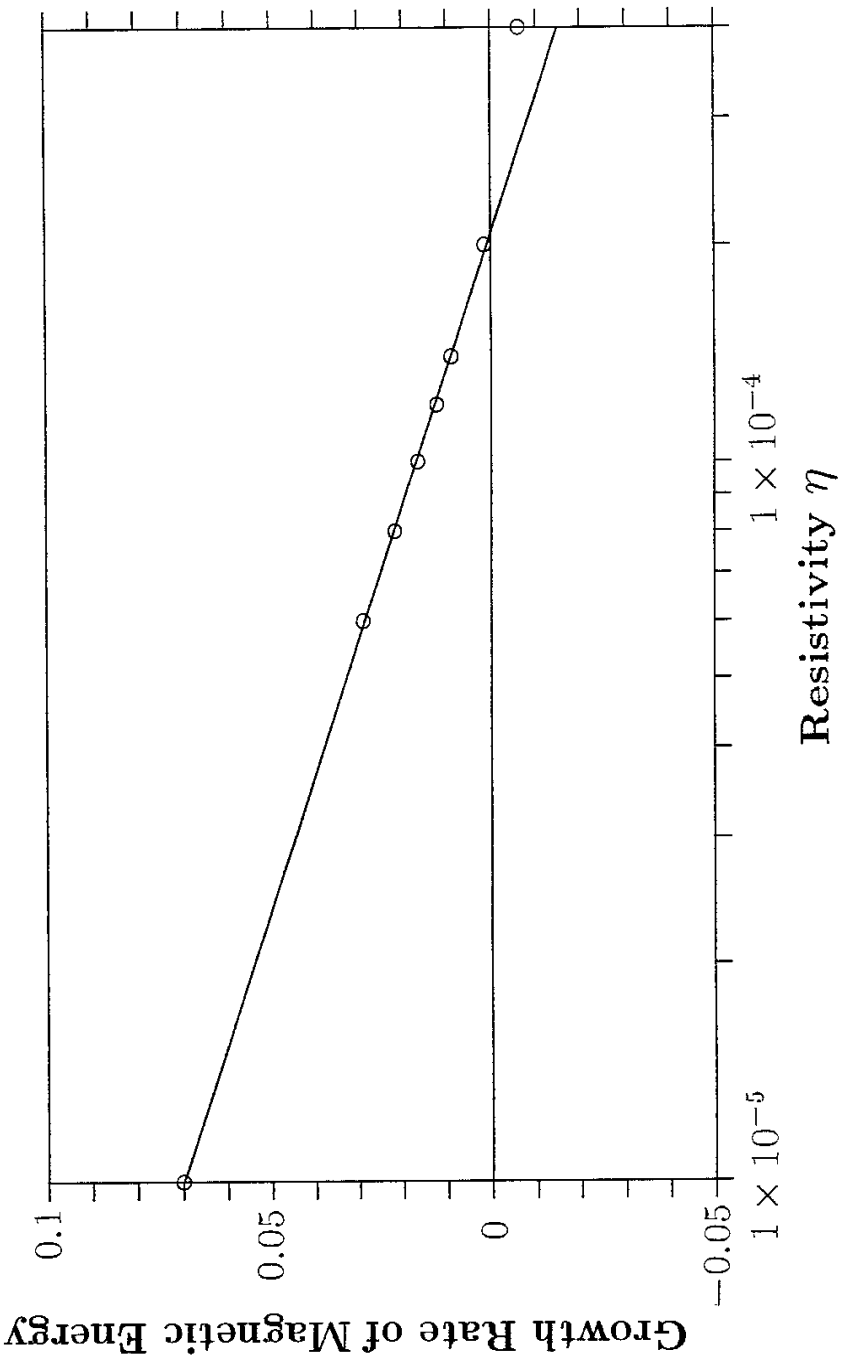
Growth Rate of Magnetic Energy
0.1
0.05
0
−0.05
1×10^{-5}
1×10^{-4}
Resistivity η

Fig. 2

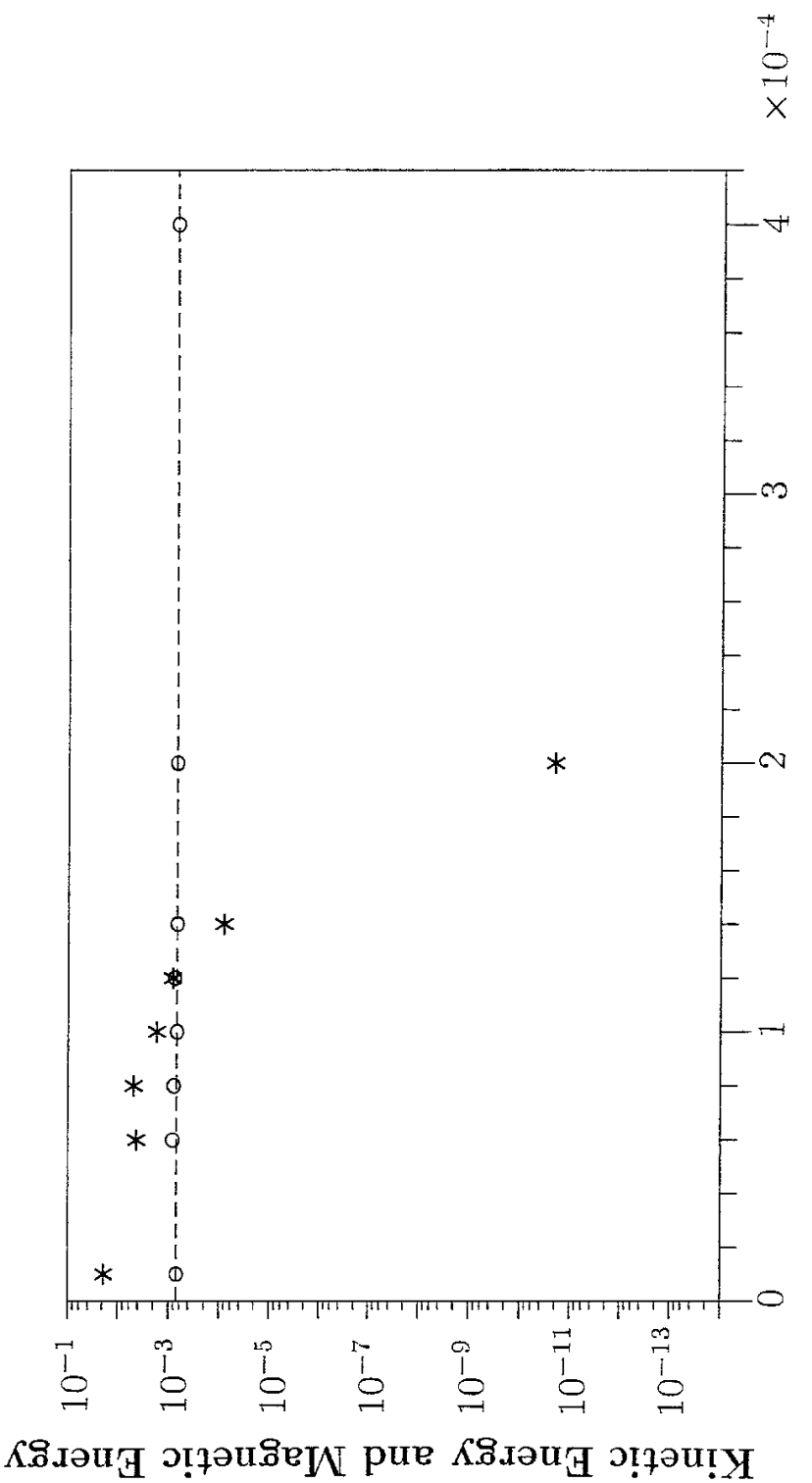
Kinetic Energy and Magnetic Energy
10^{-1}
10^{-3}
10^{-5}
10^{-7}
10^{-9}
10^{-11}
10^{-13}
0
1
2
3
4
$\times 10^{-4}$
Resistivity

Fig. 3

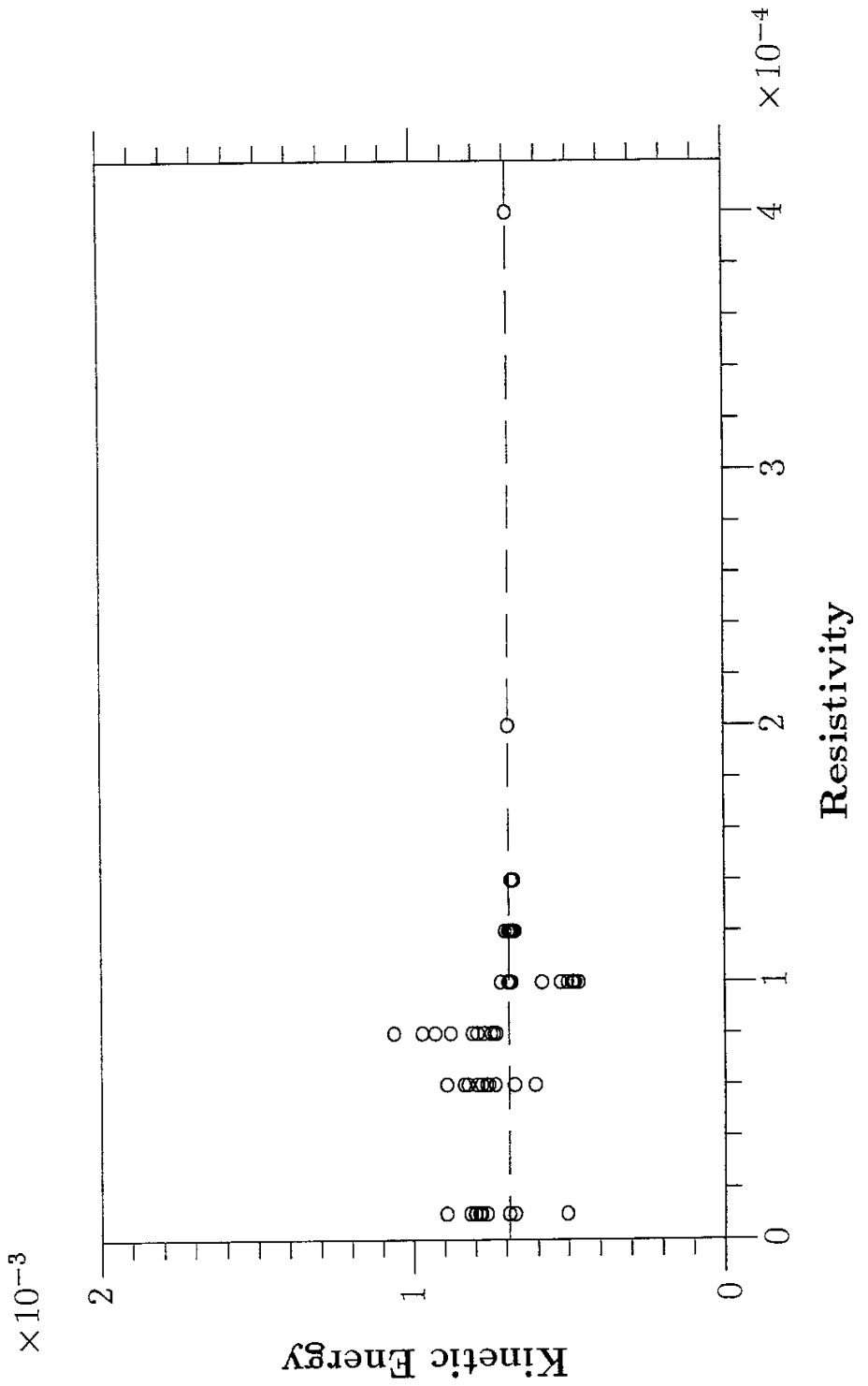

Fig. 4

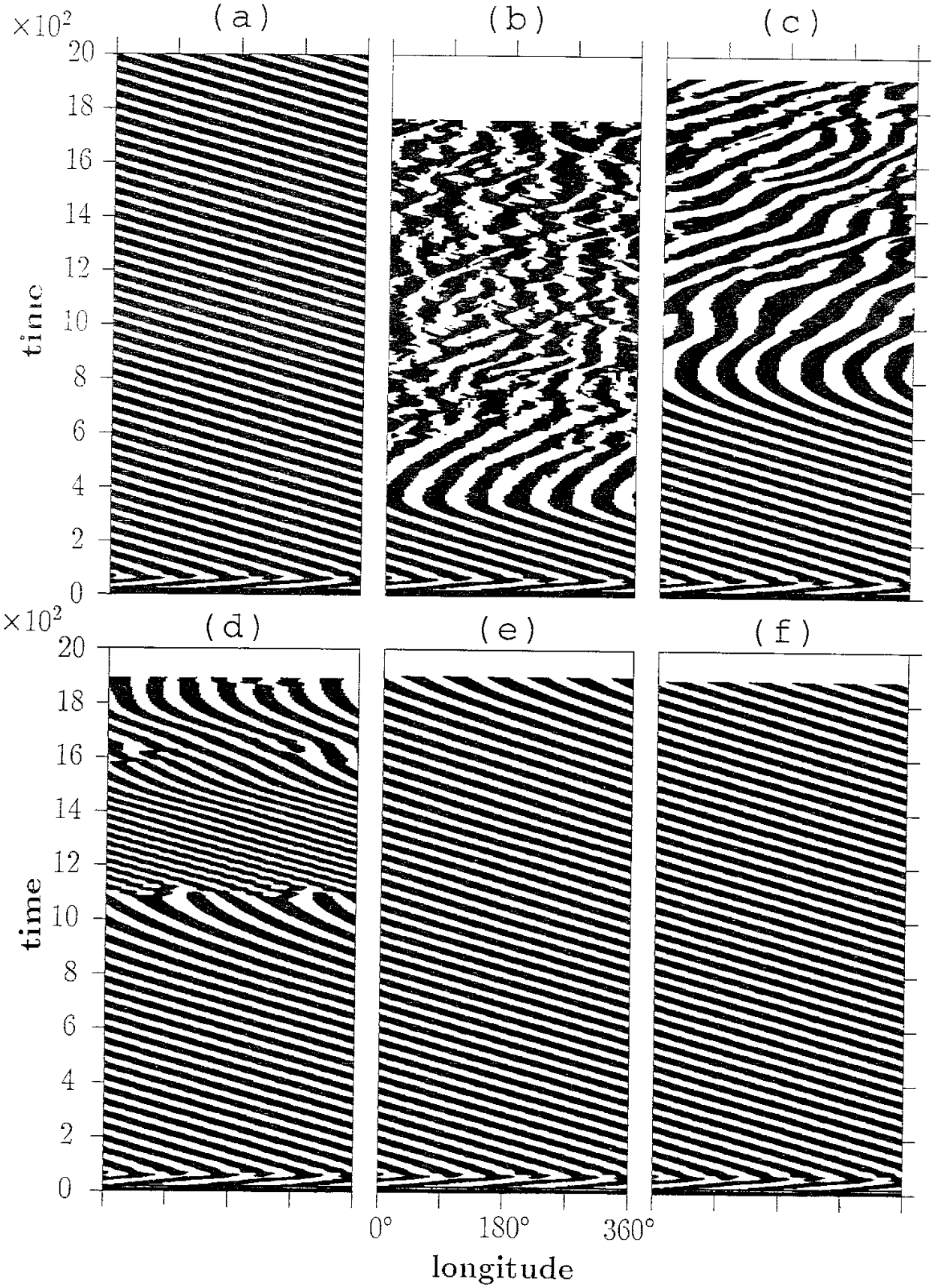

Fig. 5

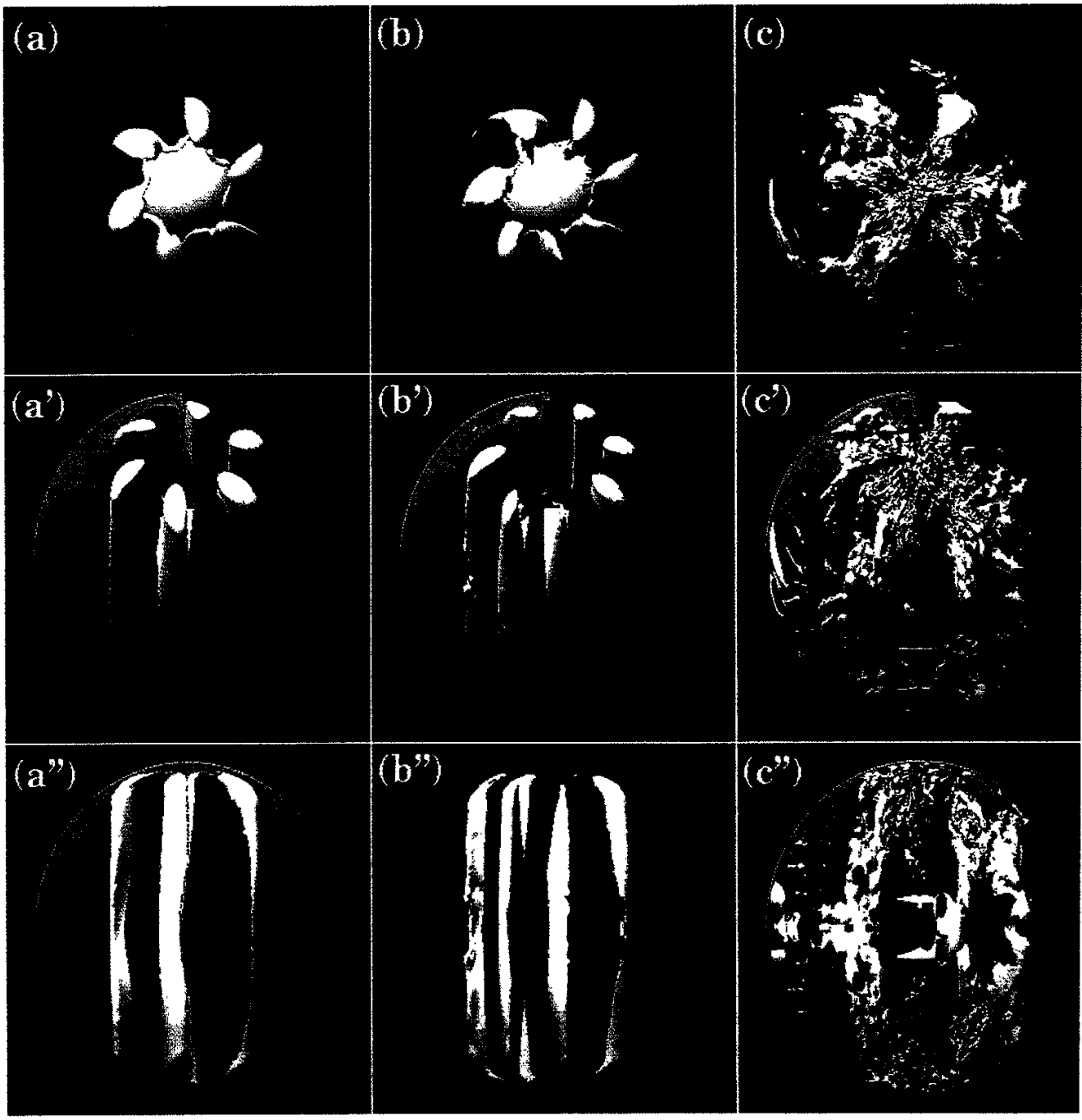

Fig. 6

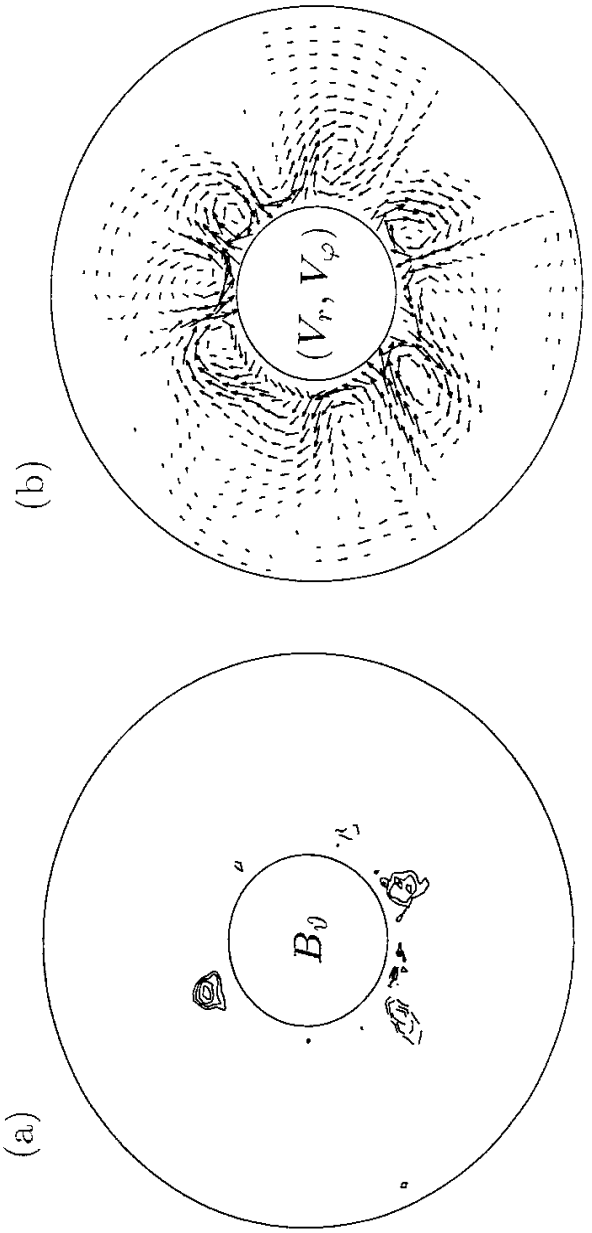

Fig. 7

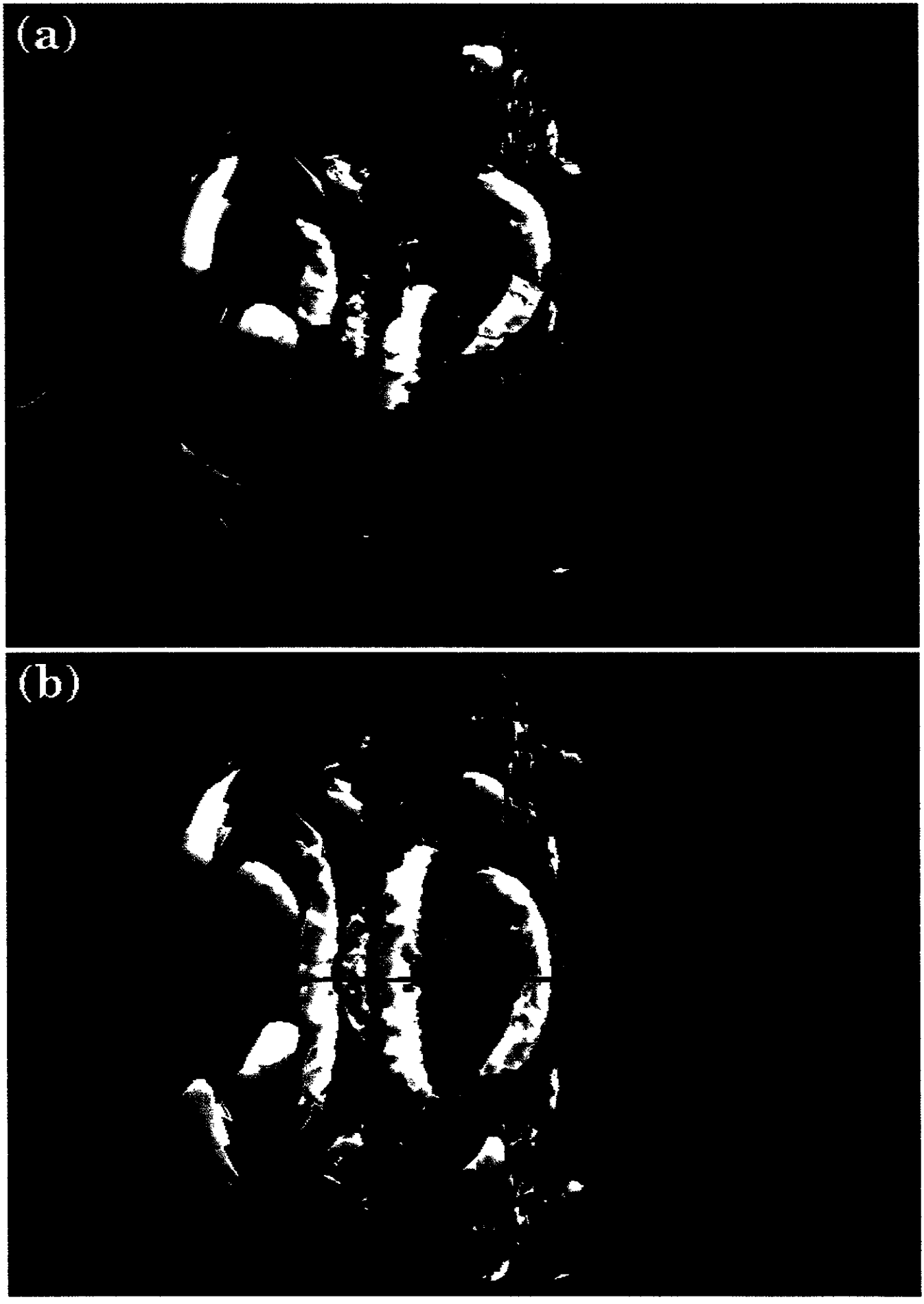

Fig. 8

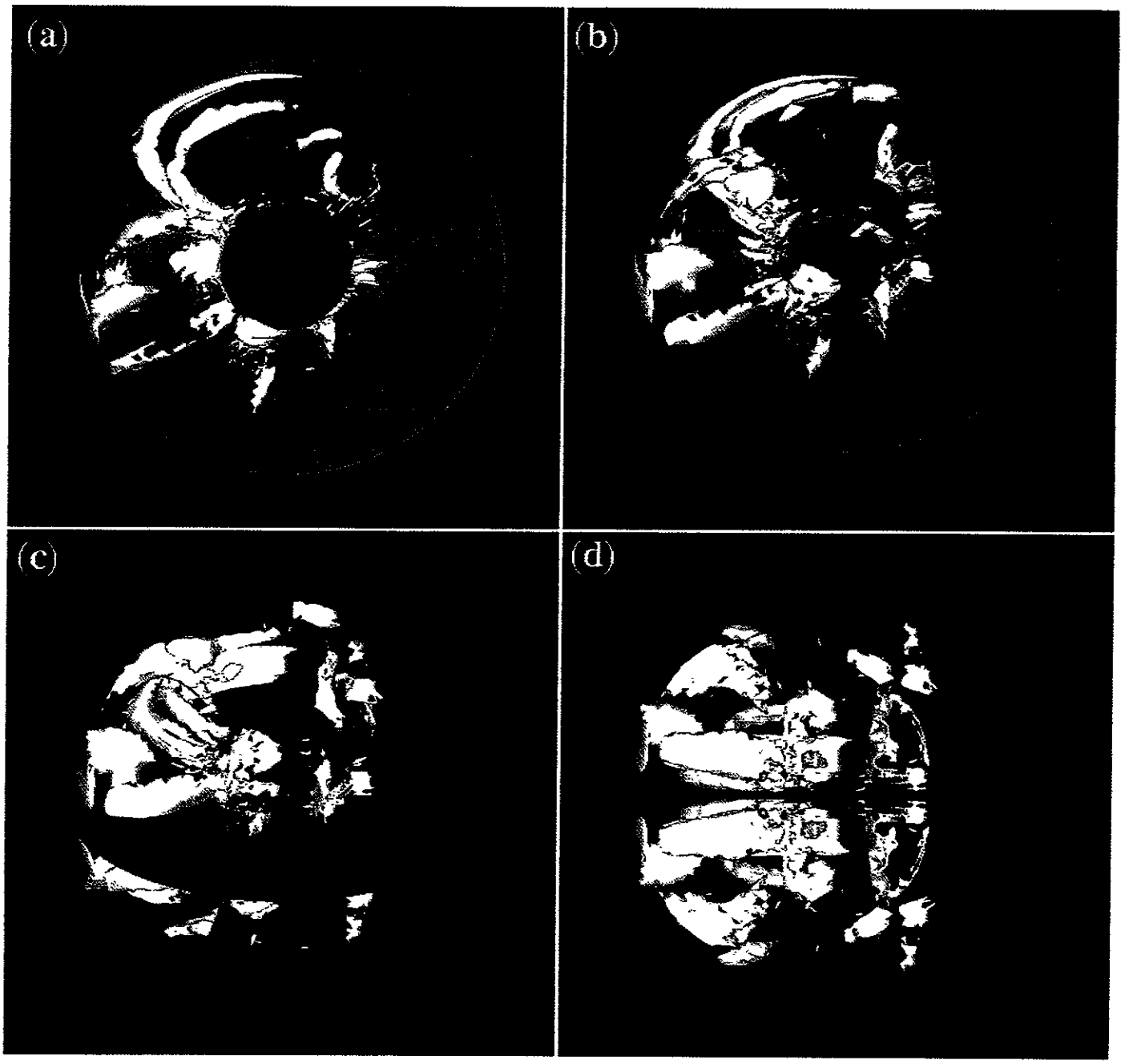

Fig. 9

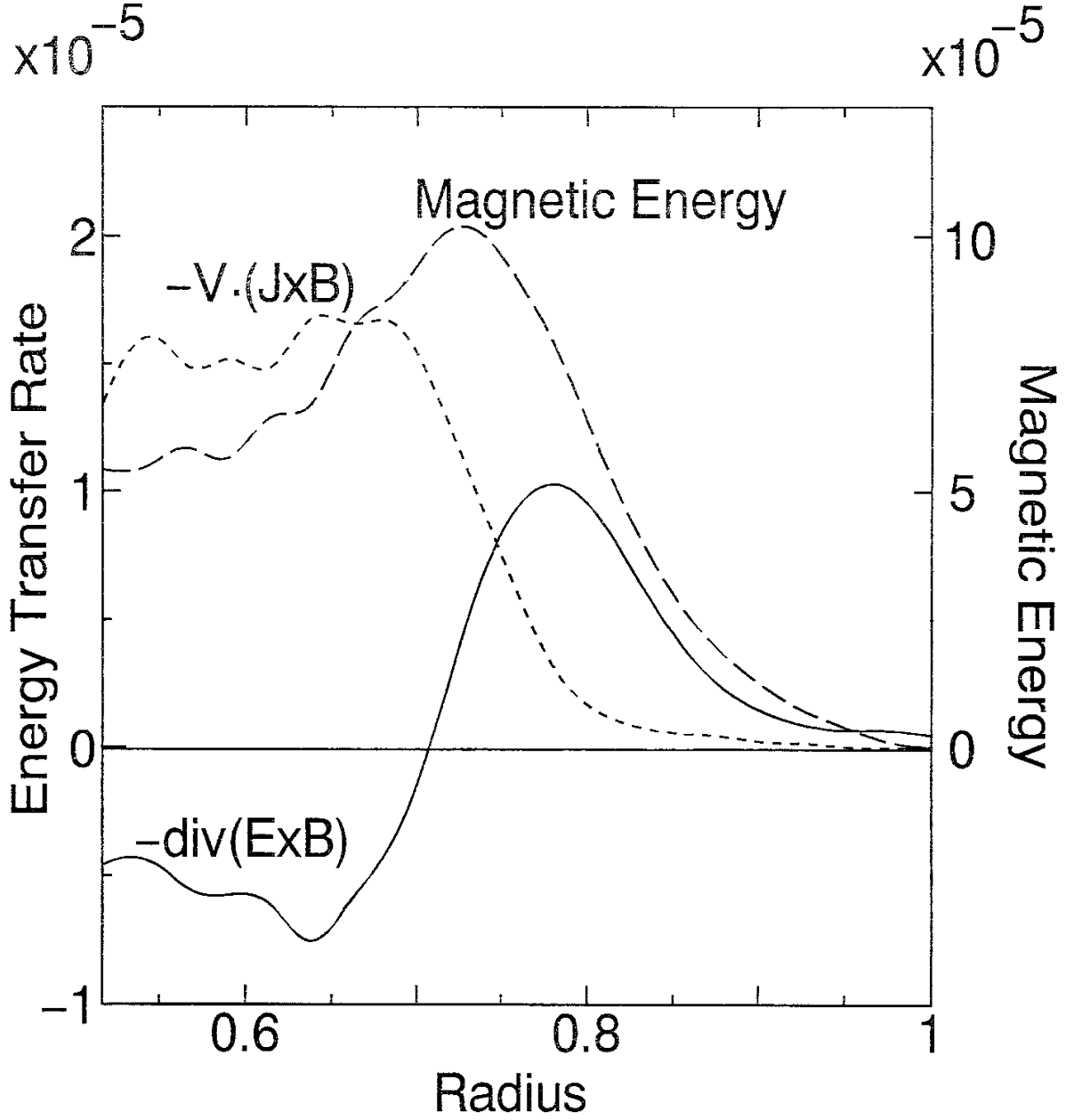
x10^-5
x10^-5
Magnetic Energy
-V·(JxB)
-div(ExB)
Energy Transfer Rate
Magnetic Energy
2
1
0
-1
10
5
0
0.6
0.8
1
Radius

Fig. 10

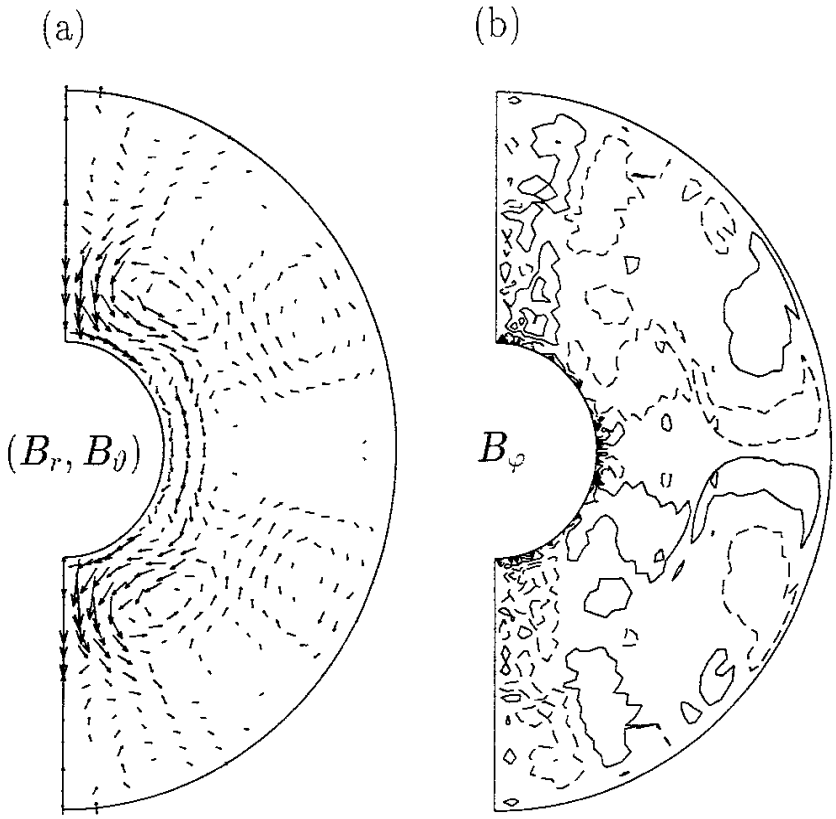

Fig. 11

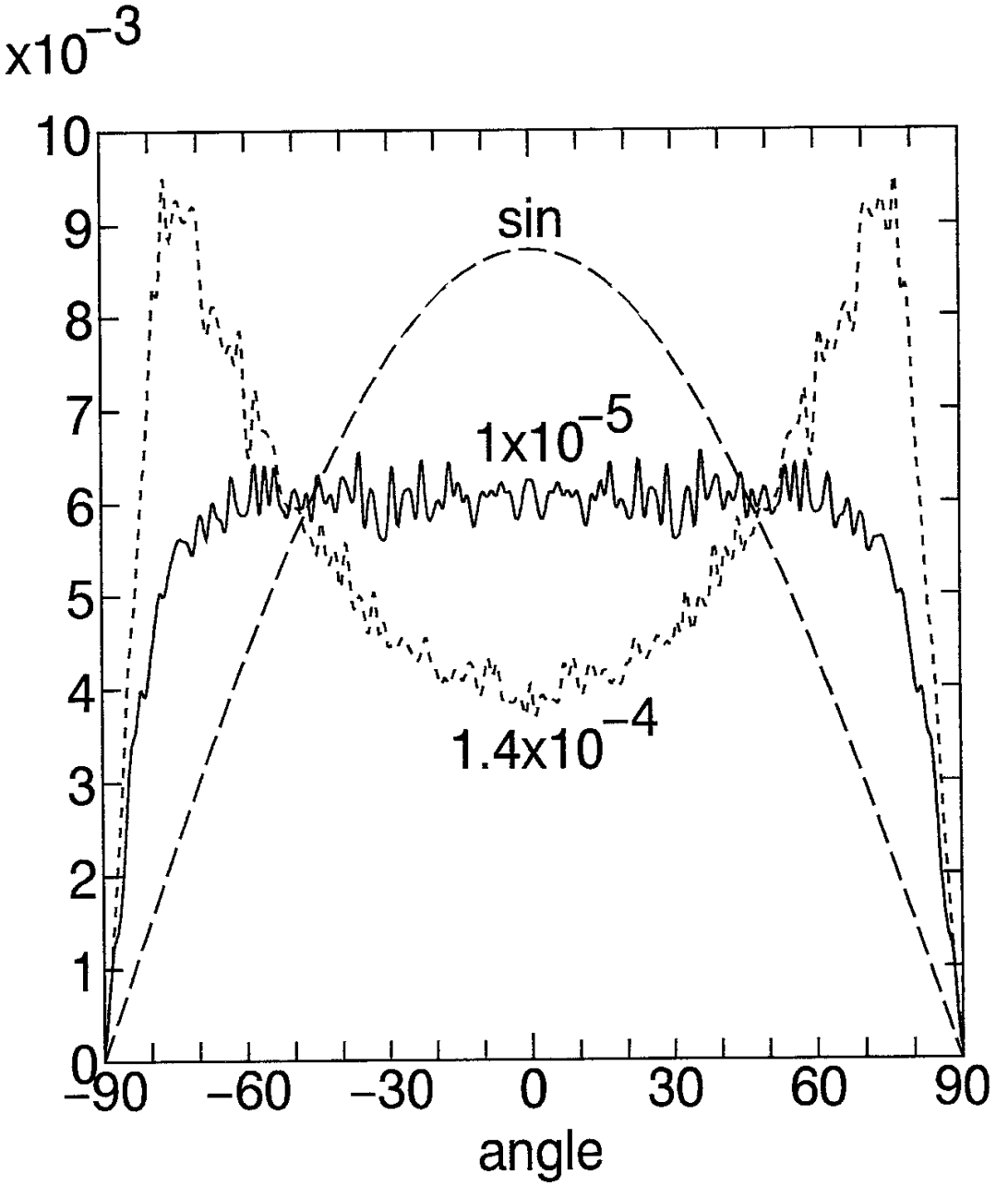

Fig. 12

Recent Issues of NIFS Series

NIFS-281 K. Kamada, H. Kinoshita and H. Takahashi,
Anomalous Heat Evolution of Deuteron Implanted Al on Electron Bombardment ; May 1994

NIFS-282 H. Takamaru, T. Sato, K. Watanabe and R. Horiuchi,
Super Ion Acoustic Double Layer; May 1994

NIFS-283 O.Mitarai and S. Sudo,
Ignition Characteristics in D-T Helical Reactors; June 1994

NIFS-284 R. Horiuchi and T. Sato,
Particle Simulation Study of Driven Magnetic Reconnection in a Collisionless Plasma; June 1994

NIFS-285 K.Y. Watanabe, N. Nakajima, M. Okamoto, K. Yamazaki, Y. Nakamura, M. Wakatani,
Effect of Collisionality and Radial Electric Field on Bootstrap Current in LHD (Large Helical Device); June 1994

NIFS-286 H. Sanuki, K. Itoh, J. Todoroki, K. Ida, H. Idei, H. Iguchi and H. Yamada,
Theoretical and Experimental Studies on Electric Field and Confinement in Helical Systems; June 1994

NIFS-287 K. Itoh and S-I. Itoh,
Influence of the Wall Material on the H-mode Performance; June 1994

NIFS-288 K. Itoh, A. Fukuyama, S.-I. Itoh, M. Yagi and M. Azumi,
Self-Sustained Magnetic Braiding in Toroidal Plasmas: July 1994

NIFS-289 Y. Nejoh,
Relativistic Effects on Large Amplitude Nonlinear Langmuir Waves in a Two-Fluid Plasma; July 1994

NIFS-290 N. Ohyabu, A. Komori, K. Akaishi, N. Inoue, Y. Kubota, A.I. Livshit, N. Noda, A. Sagara, H. Suzuki, T. Watanabe, O. Motojima, M. Fujiwara, A. Iiyoshi,
Innovative Divertor Concepts for LHD; July 1994

NIFS-291 H. Idei, K. Ida, H. Sanuki, S. Kubo, H. Yamada, H. Iguchi, S. Morita, S. Okamura, R. Akiyama, H. Arimoto, K. Matsuoka, K. Nishimura, K. Ohkubo, C. Takahashi, Y. Takita, K. Toi, K. Tsumori and I. Yamada,
Formation of Positive Radial Electric Field by Electron Cyclotron Heating in Compact Helical System; July 1994

NIFS-292 N. Noda, A. Sagara, H. Yamada, Y. Kubota, N. Inoue, K. Akaishi, O. Motojima,

K. Iwamoto, M. Hashiba, I. Fujita, T. Hino, T. Yamashina, K. Okazaki, J. Rice, M. Yamage, H. Toyoda and H. Sugai,
Boronization Study for Application to Large Helical Device; July 1994

NIFS-293 Y. Ueda, T. Tanabe, V. Philipps, L. Könen, A. Pospieszczyk, U. Samm, B. Schweer, B. Unterberg, M. Wada, N. Hawkes and N. Noda,
Effects of Impurities Released from High Z Test Limiter on Plasma Performance in TEXTOR; July. 1994

NIFS-294 K. Akaishi, Y. Kubota, K. Ezaki and O. Motojima,
Experimental Study on Scaling Law of Outgassing Rate with A Pumping Parameter, Aug. 1994

NIFS-295 S. Bazdenkov, T. Sato, R. Horiuchi, K. Watanabe,
Magnetic Mirror Effect as a Trigger of Collisionless Magnetic Reconnection, Aug. 1994

NIFS-296 K. Itoh, M. Yagi, S.-I. Itoh, A. Fukuyama, H. Sanuki, M. Azumi,
Anomalous Transport Theory for Toroidal Helical Plasmas,
Aug. 1994 (IAEA-CN-60/D-III-3)

NIFS-297 J. Yamamoto, O. Motojima, T. Mito, K. Takahata, N. Yanagi, S. Yamada, H. Chikaraishi, S. Imagawa, A. Iwamoto, H. Kaneko, A. Nishimura, S. Satoh, T. Satow, H. Tamura, S. Yamaguchi, K. Yamazaki, M. Fujiwara, A. Iiyoshi and LHD group,
New Evaluation Method of Superconductor Characteristics for Realizing the Large Helical Device; Aug. 1994 (IAEA-CN-60/F-P-3)

NIFS-298 A. Komori, N. Ohyabu, T. Watanabe, H. Suzuki, A. Sagara, N. Noda, K. Akaishi, N. Inoue, Y. Kubota, O Motojima, M. Fujiwara and A. Iiyoshi,
Local Island Divertor Concept for LHD; Aug. 1994 (IAEA-CN-60/F-P-4)

NIFS-299 K. Toi, T. Morisaki, S. Sakakibara, A. Ejiri, H. Yamada, S. Morita, K. Tanaka, N. Nakajima, S. Okamura, H. Iguchi, K. Ida, K. Tsumori, S. Ohdachi, K. Nishimura, K. Matsuoka, J. Xu, I. Yamada, T. Minami, K. Narihara, R. Akiyama, A. Ando, H. Arimoto, A. Fujisawa, M. Fujiwara, H. Idei, O. Kaneko, K. Kawahata, A. Komori, S. Kubo, R. Kumazawa, T. Ozaki, A. Sagara, C. Takahashi, Y. Takita and T. Watari,
Impact of Rotational-Transform Profile Control on Plasma Confinement and Stability in CHS; Aug. 1994 (IAEA-CN-60/A6/C-P-3)

NIFS-300 H. Sugama and W. Horton,
Dynamical Model of Pressure-Gradient-Driven Turbulence and Shear Flow Generation in L-H Transition; Aug. 1994 (IAEA/CN-60/D-P-I-11)

NIFS-301 Y. Hamada, A. Nishizawa, Y. Kawasumi, K.N. Sato, H. Sakakita, R. Liang, K. Kawahata, A. Ejiri, K. Narihara, K. Sato, T. Seki, K. Toi, K. Itoh, H. Iguchi, A. Fujisawa, K. Adachi, S. Hidekuma, S. Hirokura, K. Ida, M. Kojima, J. Koog, R. Kumazawa, H. Kuramoto, T. Minami, I. Negi,

S. Ohdachi, M. Sasao, T. Tsuzuki, J. Xu, I. Yamada, T. Watari,
Study of Turbulence and Plasma Potential in JIPP T-IIU Tokamak;
Aug. 1994 (IAEA/CN-60/A-2-III-5)

NIFS-302 K. Nishimura, R. Kumazawa, T. Mutoh, T. Watari, T. Seki, A. Ando, S. Masuda, F. Shinpo, S. Murakami, S. Okamura, H. Yamada, K. Matsuoka, S. Morita, T. Ozaki, K. Ida, H. Iguchi, I. Yamada, A. Ejiri, H. Idei, S. Muto, K. Tanaka, J. Xu, R. Akiyama, H. Arimoto, M. Isobe, M. Iwase, O. Kaneko, S. Kubo, T. Kawamoto, A. Lazaros, T. Morisaki, S. Sakakibara, Y. Takita, C. Takahashi and K. Tsumori,
ICRF Heating in CHS; Sep. 1994 (IAEA-CN-60/A-6-I-4)

NIFS-303 S. Okamura, K. Matsuoka, K. Nishimura, K. Tsumori, R. Akiyama, S. Sakakibara, H. Yamada, S. Morita, T. Morisaki, N. Nakajima, K. Tanaka, J. Xu, K. Ida, H. Iguchi, A. Lazaros, T. Ozaki, H. Arimoto, A. Ejiri, M. Fujiwara, H. Idei, A. Iiyoshi, O, Kaneko, K. Kawahata, T. Kawamoto, S. Kubo, T. Kuroda, O. Motojima, V.D. Pustovitov, A. Sagara, C. Takahashi, K. Toi and I. Yamada,
High Beta Experiments in CHS; Sep. 1994 (IAEA-CN-60/A-2-IV-3)

NIFS-304 K. Ida, H. Idei, H. Sanuki, K. Itoh, J. Xu, S. Hidekuma, K. Kondo, A. Sahara, H. Zushi, S.-I. Itoh, A. Fukuyama, K. Adati, R. Akiyama, S. Bessho, A. Ejiri, A. Fujisawa, M. Fujiwara, Y. Hamada, S. Hirokura, H. Iguchi, O. Kaneko, K. Kawahata, Y. Kawasumi, M. Kojima, S. Kubo, H. Kuramoto, A. Lazaros, R. Liang, K. Matsuoka, T. Minami, T. Mizuuchi, T. Morisaki, S. Morita, K. Nagasaki, K. Narihara, K. Nishimura, A. Nishizawa, T. Obiki, H. Okada, S. Okamura, T. Ozaki, S. Sakakibara, H. Sakakita, A. Sagara, F. Sano, M. Sasao, K. Sato, K.N. Sato, T. Saeki, S. Sudo, C. Takahashi, K. Tanaka, K. Tsumori, H.Yamada, I. Yamada, Y. Takita, T. Tuzuki, K. Toi and T. Watari,
Control of Radial Electric Field in Torus Plasma; Sep. 1994
(IAEA-CN-60/A-2-IV-2)

NIFS-305 T. Hayashi, T. Sato, N. Nakajima, K. Ichiguchi, P. Merkel, J. Nührenberg, U. Schwenn, H. Gardner, A. Bhattacharjee and C.C.Hegna,
Behavior of Magnetic Islands in 3D MHD Equilibria of Helical Devices;
Sep. 1994 (IAEA-CN-60/D-2-II-4)

NIFS-306 S. Murakami, M. Okamoto, N. Nakajima, K.Y. Watanabe, T. Watari, T. Mutoh, R. Kumazawa and T. Seki,
Monte Carlo Simulation for ICRF Heating in Heliotron/Torsatrons;
Sep. 1994 (IAEA-CN-60/D-P-I-14)

NIFS-307 Y. Takeiri, A. Ando, O. Kaneko, Y. Oka, K. Tsumori, R. Akiyama, E. Asano, T. Kawamoto, T. Kuroda, M. Tanaka and H. Kawakami,
Development of an Intense Negative Hydrogen Ion Source with a Wide-Range of External Magnetic Filter Field; Sep. 1994

NIFS-308 T. Hayashi, T. Sato, H.J. Gardner and J.D. Meiss,
Evolution of Magnetic Islands in a Heliac; Sep. 1994

NIFS-309 H. Amo, T. Sato and A. Kageyama,
Intermittent Energy Bursts and Recurrent Topological Change of a Twisting Magnetic Flux Tube; Sep.1994

NIFS-310 T. Yamagishi and H. Sanuki,
Effect of Anomalous Plasma Transport on Radial Electric Field in Torsatron/Heliotron; Sep. 1994

NIFS-311 K. Watanabe, T. Sato and Y. Nakayama,
Current-profile Flattening and Hot Core Shift due to the Nonlinear Development of Resistive Kink Mode; Oct. 1994

NIFS-312 M. Salimullah, B. Dasgupta, K. Watanabe and T. Sato,
Modification and Damping of Alfvén Waves in a Magnetized Dusty Plasma; Oct. 1994

NIFS-313 K. Ida, Y. Miura, S -I. Itoh, J.V. Hofmann, A. Fukuyama, S. Hidekuma, H. Sanuki, H. Idei, H. Yamada, H. Iguchi, K. Itoh,
Physical Mechanism Determining the Radial Electric Field and its Radial Structure in a Toroidal Plasma; Oct. 1994

NIFS-314 Shao-ping Zhu, R. Horiuchi, T. Sato and The Complexity Simulation Group,
Non-Taylor Magnetohydrodynamic Self-Organization; Oct. 1994

NIFS-315 M. Tanaka,
Collisionless Magnetic Reconnection Associated with Coalescence of Flux Bundles; Nov. 1994

NIFS-316 M. Tanaka,
Macro-EM Particle Simulation Method and A Study of Collisionless Magnetic Reconnection; Nov. 1994

NIFS-317 A. Fujisawa, H. Iguchi, M. Sasao and Y. Hamada,
Second Order Focusing Property of 210 ° Cylindrical Energy Analyzer; Nov. 1994

NIFS-318 T. Sato and Complexity Simulation Group,
Complexity in Plasma - A Grand View of Self- Organization; Nov. 1994

NIFS-319 Y. Todo, T. Sato, K. Watanabe, T.H. Watanabe and R. Horiuchi,
MHD-Vlasov Simulation of the Toroidal Alfvén Eigenmode; Nov. 1994